24th INTERNATIONAL CONGRESS ON SOUND AND VIBRATION
23–27 July 2017, London

ICSV24
23-27JULY 2017
LONDON CALLING

VIBRATION AND SOUND OF A HIGHLY-ELASTIC THIN AIRFOIL

Avshalom Manela and Michael Weidenfeld
Technion, Faculty of Aerospace Engineering, Haifa, Israel
email: amanela@technion.ac.il

We investigate the near and far fields of a thin elastic filament set at uniform low-Mach flow and subject to leading-edge heaving actuation. The filament is "hanged" in the vertical direction and is free at its downstream end, so that "hanging chain" gravity-induced tension forces apply. The filament bending rigidity is assumed small, and we focus on analyzing the differences between a highly elastic structure and a membrane (where the bending rigidity vanishes). The near field is studied based on potential thin airfoil theory, whereas the acoustic field is investigated using the Powell-Howe acoustic analogy. The results shed light on the specific effect of structure bending stiffness on the dynamics and acoustic disturbance of an airfoil.

1. Introduction

The “hanging chain" problem, considering the *in vacuo* motion of a string suspended at its upper end, free at its lower end, and subject to a downward gravity force, is a classical problem in structural dynamics that has been studied extensively over the years [1]. The problem has been first considered by Daniel Bernoulli during the 18th century, who used it as a model case for introducing the Bessel eigenfunctions. Ever since, it has served as a useful setup for analyzing the small- and large-amplitude vibrations developed in thin non-stiff bodies that are subject to external forcing (e.g., [2, 3]). In the original formulation of the problem, the chain dynamic balance consists of body inertia and gravity-driven tension, while the impact of structural bending rigidity is omitted. Yet, this latter effect always exists, even if to a limited extent, and is known to have crucial importance in various applications in civil and mechanical engineering [1, 4].

From a mathematical point of view, inclusion of the bending rigidity effect, even in a linearized formulation, fundamentally changes the problem type from second to higher order in space, and imposes the satisfaction of additional end-point conditions. In an effort to analyze the singular impact of this change, several works have investigated the eigen- and external-force-induced motions of an elastic beam in the limit of small bending stiffness [5, 6, 7], applying asymptotic and numerical methods in the process of analysis. Notably, all of these studies have considered *in vacuo* setups, where no consideration has been taken of the coupling with surrounding media. Even so, the problem in hand was found challenging enough so that no complete analytical investigation could be carried out, and the “patching" of an outer numerical solution with inner asymptotic approximations had to be employed [7].

In parallel with the above investigations, a large number of works have recently analyzed a geometrically similar, yet fundamentally different, “flapping flag" problem, where the fluid-structure interaction of a thin filament with uniform incoming flow is considered (see Refs. [8, 9] and references cited therein). This model problem has been shown relevant in a variety of engineering applications, including the development of energy harvesting methodologies [10], optimization of propulsion performance in single-body and group environments [11, 12], the mechanical modeling of palatal snoring [13], and the evaluation of aerodynamic sound during flapping flight [14, 15]. In a typical setup, no

account is taken of gravity effects (unless a more involved three-dimensional problem is considered [16]), and the flag is modeled as an elastic fixed-free beam. When considering the linearized problem, all tension forces are neglected, and the leading-order dynamic balance consists of inertia, bending rigidity, and fluid loading effects.

Inasmuch as structural rigidity is always present in a hanging chain setup, it may be argued that tension forces always exist in a flapping flag configuration. Such forces may originate from either structure-induced effects (to maintain filament inextensibility), viscous boundary layer loading, or any other external forcing acting parallel to the unperturbed body state. In the small-amplitude regime, it may be shown that the effect of structure-induced tension is of higher order [17], and may thus be neglected. Additionally, the relatively small magnitude of drag-induced tension at high Reynolds number flows makes its impact minor [18]. To consider the third type of an externally-induced tension, Datta and Gottenberg [19] have studied the free vibrations developed in an infinitely long elastic strip hanging vertically in a downward stream. A simplified “slender body" description has been applied to model the pressure loading acting on the body. This model essentially neglects the effects of downstream wake and filament end points on the developed motion. A similar theoretical approach has been applied later on, and validated experimentally, by Lemaitre *et al.* [20], to analyze the flutter instability of a long ribbon hanging in axial air flow.

Noting the above, the objective of the present work is to investigate the motion of a finite-chord flag immersed in uniform mean flow and subject to a gravity force in its axial direction. We focus on the limit of small structural bending rigidity, to contrast the dynamic response of a membrane (having no bending rigidity) with an elastic beam. For an elastic “flag", such an investigation is of particular interest, since the typical rigidity involved (proportional to the third power of the filament thickness) is arguably very small. In contrast with previous studies, the present analysis takes account of the end effects of the body, and fully models the wake generated by the filament interaction with the flow. This enables investigation of the impact of the difference in boundary conditions (between the membrane and the beam) on the results, and allows quantitative discussion of the end-layer type of motion observed near the flag edges.

2. Formulation of the problem

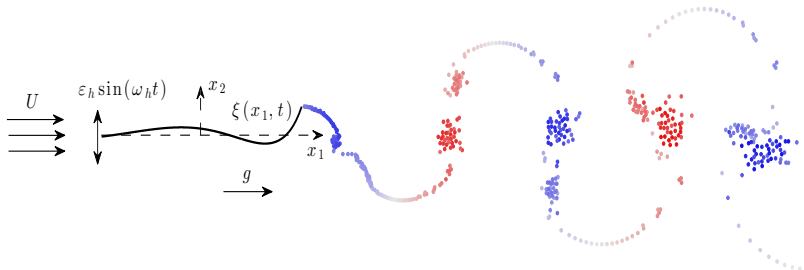

Figure 1: Schematic of the hanging-flag setup: A flexible filament of length $2a$ is hanging in uniform flow of speed U at zero incidence, and actuated at its upstream end with small-amplitude heaving motion. A wake, composed of discrete point vortices with positive (red) and negative (blue) circulations, emanates from the filament downstream end.

The problem setup is described in Fig. 1. Consider a two-dimensional thin elastic filament of length $2a$, mass per unit area ρ_s, and bending rigidity EI. The filament is immersed in uniform flow of

speed U in the x_1-direction, and is subject to a gravity body force, $\mathbf{g} = g\hat{\mathbf{x}}_\mathbf{1}$. At time $t \geq 0$, sinusoidal heaving actuation is applied at the structure upstream end,

$$\xi(x_1 = -a) = \bar{\varepsilon}_h a \sin(\omega_h t). \tag{1}$$

In (1), $\xi(x_1, t)$ marks the filament displacement in the x_2-direction, $\bar{\varepsilon}_h \ll 1$ (with an overbear marking a non-dimensional quantity) is the scaled heaving amplitude, and ω_h denotes the prescribed heaving frequency. In line with hanging chain theory, the gravity-driven tensile force acting on the filament per unit length is independent of structure vibrations, and is given by

$$T(x_1) = \rho_s g (a - x_1). \tag{2}$$

The tension acquires its maximal value (equal to the filament total mass per unit length) at the actuated edge $x_1 = -a$, and vanishes at the free end $x_1 = a$. Based on the above description, the filament displacement $\xi(x_1, t)$ is governed by the linearized equation of motion

$$\rho_s \frac{\partial^2 \xi}{\partial t^2} + EI \frac{\partial^4 \xi}{\partial x_1^4} - \rho_s g \frac{\partial}{\partial x_1}\left((a - x_1)\frac{\partial \xi}{\partial x_1}\right) = \Delta p(x_1, t), \tag{3}$$

balancing structural inertia, bending stiffness, tensile force, and fluid loading terms. On the right-hand side, $\Delta p = p_- - p_+$ marks fluid pressure jump between the filament lower (p_-) and upper (p_+) surfaces. It is through this term, missing in previous analyses of the *in vacuo* hanging chain problem, that the structure motion and fluid dynamical problems are coupled.

Assuming high Reynolds number conditions, we consider the flow field to be inviscid. The small amplitude of filament deflections (see Eq. (1)) then allows for the application of potential thin airfoil theory to describe the fluid dynamical problem. In line with the unsteady conditions considered and the Kelvin theorem, continuous vortex shedding occurs at the structure surface. At the small angles of attack assumed, the flow at the filament upstream end and along its chord is regarded attached, and release of vorticity is allowed only at the structure downstream edge. To describe the time evolution of filament wake, we make use of a discrete-vortex representation, where, at each time step, a concentrated line vortex is released to the flow, with its strength Γ_k fixed by the Kelvin theorem and the instantaneous time change in filament circulation (see Fig. 1). While discrete models are known to be sensitive to the initial locations and core modeling of the nascent vortex [21, 22], our results indicate, to the extent that the present small-amplitude setup is considered, that the chosen wake description is converged in both time and space. At each time step Δt, the nascent point vortex is placed at a distance $U\Delta t$ in the mean-flow direction from the instantaneous position of the trailing edge. Once released, the trajectory of each wake vortex follows from a potential-flow calculation, as formulated below (see Eq. (8)).

Adopting the thin-airfoil methodology, the filament is represented through its circulation distribution per unit length, $\gamma(x_1, t)$. Applying a complex notation and denoting the conjugate velocity of the potential flow-field by $W(z)$, the impermeability condition takes the form

$$\frac{\partial \xi}{\partial t} + U \frac{\partial \xi}{\partial x_1} = -\mathrm{Im}\{W(z)|_{-a \leq x_1 \leq a}\}, \tag{4}$$

where

$$W(z) = U - \frac{i}{2\pi}\left(\sum_{k=1}^{N} \frac{\Gamma_k}{z - z_{\Gamma_k}} + \int_{-a}^{a} \frac{\gamma(s,t)\,\mathrm{d}s}{z - s}\right). \tag{5}$$

At the filament surface

$$W(z)|_{-a \leq x_1 \leq a} = U - \frac{i}{2\pi}\left(\sum_{k=1}^{N} \frac{\Gamma_k}{x_1 - z_{\Gamma_k}} + \fint_{-a}^{a} \frac{\gamma(s,t)\,\mathrm{d}s}{x_1 - s}\right), \tag{6}$$

where the barred integral sign denotes a Cauchy principal value integral. In (4)-(6), $z = x_1 + \mathrm{i}x_2$ marks the complex representation of a point in the plane of motion, and z_{Γ_k} denotes the instantaneous location of the k-th trailing edge vortex. The pressure jump Δp across the filament, appearing in the filament equation of motion (3), is determined by the unsteady Bernoulli's equation,

$$\Delta p(x_1, t) = \rho_0 U \gamma(x_1, t) + \rho_0 \frac{\partial}{\partial t} \int_{-a}^{x_1} \gamma(s, t)\, \mathrm{d}s, \tag{7}$$

where ρ_0 denotes the fluid mean density.

Wake vortices dynamics is coupled to the system through the right-hand side of the impermeability condition (4). In line with potential-flow theory, the motion of each of these vortices is governed by

$$\frac{\mathrm{d}z_{\Gamma_k}}{\mathrm{d}t} = W^*_{\Gamma_k} \quad (k = 1, 2, \ldots, N), \tag{8}$$

where $W^*_{\Gamma_k}$ marks the complex conjugate of the conjugate velocity induced at the instantaneous location of the k-th wake vortex. Removing the vortex self-singularity, $W_{\Gamma_k}(z)$ is expressed by

$$W_{\Gamma_k}(z) = U - \frac{i}{2\pi} \left(\sum_{\substack{m=1 \\ m \neq k}}^{N} \frac{\Gamma_m}{z_{\Gamma_k} - z_{\Gamma_m}} + \int_{-a}^{a} \frac{\gamma(x_1, t)\, dx_1}{z_{\Gamma_k} - x_1} \right). \tag{9}$$

The total system circulation is conserved by applying Kelvin's theorem,

$$\Gamma_N = -\left(\sum_{k=1}^{N-1} \Gamma_k + \int_{-a}^{a} \gamma(x_1, t) \mathrm{d}x_1 \right), \tag{10}$$

which fixes the strength of the nascent vortex Γ_N.

Formulation of the problem is completed by ensuring regularization of the flow-field at the filament free end through the unsteady Kutta condition, $\gamma(a, t) = 0$. Additionally, in line with the filament equation of motion (3), initial and end conditions should be specified. Assuming no structure displacements at times $t < 0$, we impose

$$\xi(x_1, 0^-) = 0\,, \left(\frac{\partial \xi}{\partial t} \right)_{(x_1, 0^-)} = 0. \tag{11}$$

Considering the upstream-end actuation in Eq. (1), and free-end conditions at $x_1 = a$, the boundary conditions applied are

$$\xi(-a, t) = \bar{\varepsilon}_h a \sin(\omega_h t)\,, \left(\frac{\partial \xi}{\partial x_1} \right)_{(-a,t)} = 0\,, \left(\frac{\partial^2 \xi}{\partial x_1^2} \right)_{(a,t)} = 0\,, \left(\frac{\partial^3 \xi}{\partial x_1^3} \right)_{(a,t)} = 0. \tag{12}$$

We assume that release of the first trailing edge vortex occurs at $t = 0$. The system evolution is then followed for $t > 0$ via numerical integration. Details regarding the problem scaling and numerical procedure are given in Sec. 3.

3. Scaling and numerical analysis

To obtain a numerical solution, the dimensional problem formulated in Sec. 2 is non-dimensionalized using the aerodynamic scales a, U, a/U, $\rho_0 U^2$ and $2\pi a U$ for the length, velocity, time, pressure and vortices circulations, respectively. Omitting presentation of the full non-dimensional problem for brevity, the scaled form of the filament equation of motion (3) is

$$\bar{\mu}\bar{\alpha} \frac{\partial^2 \bar{\xi}}{\partial \bar{t}^2} + \bar{\varepsilon} \frac{\partial^4 \bar{\xi}}{\partial \bar{x}_1^4} - \frac{\partial}{\partial \bar{x}_1} \left((1 - \bar{x}_1) \frac{\partial \bar{\xi}}{\partial \bar{x}_1} \right) = \bar{\alpha} \Delta \bar{p}, \tag{13}$$

where non-dimensional quantities are marked by overbars. The equation is accompanied by the scaled form of the boundary conditions (12),

$$\bar{\xi}(-1,\bar{t}) = \bar{\varepsilon}_h \sin(\bar{\omega}_h \bar{t}) \, , \left(\frac{\partial \bar{\xi}}{\partial \bar{x}_1}\right)_{(-1,\bar{t})} = 0 \, , \left(\frac{\partial^2 \bar{\xi}}{\partial \bar{x}_1^2}\right)_{(1,\bar{t})} = 0 \, , \left(\frac{\partial^3 \bar{\xi}}{\partial \bar{x}_1^3}\right)_{(1,\bar{t})} = 0. \tag{14}$$

Eqs. (13) and (14) are governed by the non-dimensional parameters

$$\bar{\mu} = \frac{\rho_s}{\rho_0 a} \;\; , \;\; \bar{\alpha} = \frac{\rho_0 U^2}{\rho_s g} \;\; , \;\; \bar{\varepsilon} = \frac{EI}{\rho_s g a^3} \;\; , \;\; \bar{\varepsilon}_h \text{ and } \bar{\omega}_h = \frac{a}{U}\omega_h, \tag{15}$$

denoting filament to fluid mass ratio, fluid to filament gravity-driven inertia, normalized filament rigidity, and scaled heaving amplitude and frequency, respectively. To illustrate our findings, we consider a case where $\bar{\varepsilon}_h = 0.01$, in accordance with the small-amplitude assumption set in Sec. 2, and focus on the limit of small bending stiffness, $\bar{\varepsilon} \ll 1$.

Numerical solution of the dynamical problem requires discretization of the system of equations in both space (along the filament chord) and time (from $\bar{t} = 0$ to some final time). Space discretization is needed to express the vorticity distribution $\bar{\gamma}(\bar{x}_1, \bar{t})$ along the filament, and the $\bar{x}_1$-derivatives appearing in the structure equation of motion. The numerical solution for $\bar{\gamma}(\bar{x}_1, \bar{t})$ is obtained, in each time step, via expansion of $\bar{\gamma}$ in a Fourier-type series, which identically satisfies the Kutta condition (**??**) [23]. The system of equations is then integrated in time using a fourth-order Runge-Kutta algorithm. The typical time step used for integration was $\pi/200\bar{\omega}_h$ (but not smaller than $\pi/200$ for $\bar{\omega}_h < 1$), which proved sufficient for convergence of the results. Our scheme calculates the entire time history of the system starting at $\bar{t} = 0$. Yet, for demonstrating our results, we focus on the final periodic state of the system, and not on the initial transient response. Cases where non-periodic large-amplitude motions are obtained are beyond the scope of the present work, and are not considered here.

4. Convergence of the solution at $\bar{\varepsilon} \to 0$

4.1 The problem for an actuated membrane

Focusing on the filament dynamics in the limit of small bending rigidity, we start by discussing the limit-case setup of an actuated *membrane*, where $\bar{\varepsilon} \equiv 0$. Here, the bending rigidity term is missing from the dynamical balance (13), and the small-amplitude membrane displacement $\bar{\xi}_{mem}(\bar{x}_1, \bar{t})$ (associated with the pressure jump $\Delta\bar{p}_{mem}(\bar{x}_1, \bar{t})$) is governed by

$$\bar{\mu}\bar{\alpha}\frac{\partial^2 \bar{\xi}_{mem}}{\partial \bar{t}^2} - \frac{\partial}{\partial \bar{x}_1}\left((1-\bar{x}_1)\frac{\partial \bar{\xi}_{mem}}{\partial \bar{x}_1}\right) = \bar{\alpha}\Delta\bar{p}_{mem}. \tag{16}$$

Having removed the fourth-order derivative term, only two end conditions may accompany Eq. (16). Yet, while the imposition of a heaving displacement condition at the upstream end $x_1 = -1$ is obvious, the choice for an appropriate free-end condition seems unclear in the absence of body structural stiffness. Notably, the second-derivative tension term in Eq. (16) vanishes at $\bar{x}_1 = 1$, modifying the type of the equation near the edge. Our calculations then indicate that the application of only the single heaving condition,

$$\bar{\xi}_{mem}(-1,\bar{t}) = \bar{\varepsilon}_h \sin(\bar{\omega}_h \bar{t}), \tag{17}$$

suffices to formulate a well-posed problem. Although this conclusion has been noted in previous studies of the counterpart *in vacuo* problem, it is not a trivial consequence in the present fluid-structure interaction problem. The purpose of this section is to demonstrate how the elastic filament solution at non-zero $\bar{\varepsilon} \ll 1$ converges to the membrane $\bar{\varepsilon} = 0$ solution of the problem (16)-(17).

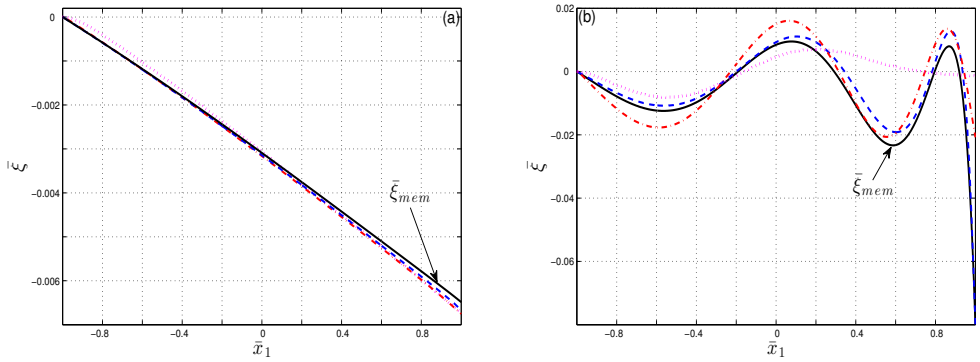

Figure 2: Numerical convergence of the filament displacement to the membrane solution at $\bar{\varepsilon} \to 0$: Comparison between the membrane deflection ($\bar{\varepsilon} = 0$, black solid lines) and the elastic filament displacement for $\bar{\varepsilon} = 10^{-6}$ (dashed blue lines), 10^{-4} (dash-dotted red lines) and 10^{-2} (dotted magenta lines), at (a) $\bar{\omega}_h = 0.5$ and (b) $\bar{\omega}_h = 5$. The results are plotted at period time, $\bar{t} = \bar{T} = 2\pi/\bar{\omega}_h$.

4.2 Comparison between the membrane and filament motions

To examine the convergence of the elastic filament solution to the membrane displacement, Figure 2 presents a comparison between the membrane $\bar{\varepsilon} = 0$ and filament deflections at decreasing values of $\bar{\varepsilon} = 10^{-2}, 10^{-4}$ and 10^{-6}. The results are plotted at period time, $\bar{t} = \bar{T} = 2\pi/\bar{\omega}_h$, for low ($\bar{\omega}_h = 0.5$, Fig. 2a) and large ($\bar{\omega}_h = 5$, Fig. 2b) values of the actuation frequency.

Starting with the low $\bar{\omega}_h = 0.5$ frequency case, we observe that the differences between the filament and membrane solutions are small at the chosen values of $\bar{\varepsilon}$. These differences are mainly confined to the vicinity of the free end, and decrease with decreasing $\bar{\varepsilon}$. This behavior changes considerably when considering the large-frequency $\bar{\omega}_h = 5$ response in Fig. 2b. Here, the amplitude of structure deflection is an order of magnitude larger than for $\bar{\omega}_h = 0.5$. In addition, the $\bar{\varepsilon} = 10^{-2}$ displacement is markedly different (and confined to a much smaller amplitude) from the membrane deflection, from which even the $\bar{\varepsilon} = 10^{-6}$ solution deviates considerably. While these deviations vanish at lower values of $\bar{\varepsilon}$ (not shown here), it is observed that the convergence of the filament to the membrane solution requires lower values of $\bar{\varepsilon}$ at larger actuation frequencies. Notably, the differences between the solutions are not confined to the vicinities of the structure end points, and are visible along the entire $-1 \le \bar{x}_1 \le 1$ filament chord.

To gain further insight into the convergence of the solution, Figs. 3a-3c compare between the membrane and filament deflections at a fixed location ($\bar{x}_1 = 1$ in Figs. 3a and 3c; $\bar{x}_1 = 0.6$ in Fig. 3b) and at the same values of $\bar{\varepsilon} = 10^{-2}, 10^{-4}$ and 10^{-6} as in Fig. 2. Additionally, Figs. 3d and 3e compare between the membrane and filament body circulations, obtained by integration over the circulation per unit length $\bar{\gamma}(\bar{x}_1, t)$ over the structure chord,

$$\bar{\Gamma}_{body}(\bar{t}) = \int_{-a}^{a} \bar{\gamma}(\bar{x}_1, \bar{t}) \mathrm{d}\bar{x}_1. \tag{18}$$

In accordance with the Kelvin theorem, $\bar{\Gamma}_{body}(\bar{t})$ is fixed by the instantaneous sum of circulations of all wake vortices (see Eq. (10)). The results are plotted along a period, $0 \le \bar{t} \le \bar{T}$, for low ($\bar{\omega}_h = 0.5$, Fig. 3a and 3d) and large ($\bar{\omega}_h = 5$, Figs. 3b, 3c and 3e) actuation frequencies.

Considering the body deflections, Fig. 3a reconfirms the results in Fig. 2a, indicating that the differences between the membrane and filament positions are negligible at the low values of $\bar{\varepsilon}$ and $\bar{\omega}_h$ considered. Figs. 3b and 3c then demonstrate the different behavior at large frequencies, characterized by considerably larger deflections, and marked differences between the membrane and various $\bar{\varepsilon} \neq 0$ displacements. These differences become larger with increasing distance from the fixed end (cf. Figs. 3b and 3c), as the position of the structure at $\bar{x}_1 = -1$ is identical in all configurations (cf. the

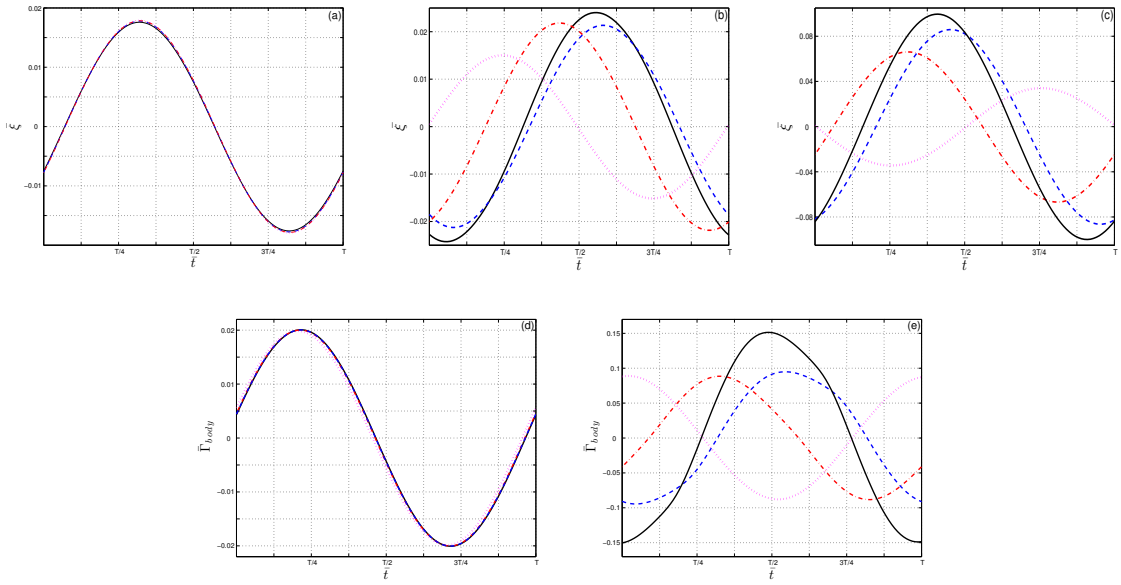

Figure 3: Numerical convergence of the filament displacement and circulation to the membrane solution at $\bar{\varepsilon} \to 0$: (a-c) Comparison between the membrane deflection ($\bar{\varepsilon} = 0$, black solid lines) and counterpart filament displacement for $\bar{\varepsilon} = 10^{-6}$ (dashed blue lines), 10^{-4} (dash-dotted red lines) and 10^{-2} (dotted magenta lines), at (a) $\bar{\omega}_h = 0.5$ and $\bar{x}_1 = 1$; (b) $\bar{\omega}_h = 5$ and $\bar{x}_1 = 0.6$; and (c) $\bar{\omega}_h = 5$ and $\bar{x}_1 = 1$. (d-e) Comparison between the membrane and filament circulations at the same values of $\bar{\varepsilon}$ for (d) $\bar{\omega}_h = 0.5$ and (e) $\bar{\omega}_h = 5$. The results are plotted along a period.

displacement conditions in Eqs. (14) and (17)). Similar trends are observed when comparing the results for the body circulation in Figs. 3d and 3e. As in Figs. 3a-3c, the differences between the membrane and filament systems are nearly indiscernible for $\bar{\omega}_h = 0.5$, but are considerable for $\bar{\omega}_h = 5$, even for $\bar{\varepsilon} = 10^{-6}$. Here, convergence of the filament to the membrane solution is obtained only at lower values of $\bar{\varepsilon}$.

Further results, demonstrating the specific effect of structural stiffness on the system behavior, as well as analysis of the resulting acoustic field, will be discussed during the presentation.

References

1. Hagedorn, P. and Dasgupta, A., *Vibrations and Waves in Continuous Mechanical Systems*, Wiley, Chichester, England (2007).

2. Bailey, H. Motion of a hanging chain after the free end is given an initial velocity, *American Journal of Physics*, **68**, 764–767, (2000).

3. Belmonte, A., Shelley, M. J., Eldakar, S. T. and Wiggins, C. H. Dynamic patterns and self-knotting of a driven hanging chain, *Physical Review Letters*, **87**, 114301, (2001).

4. Antman, S. S., *Nonlinear Problems of Elasticity*, Springer, New York (2004).

5. Lakin, W. D. Eigenvalues of a slightly stiff pendulum with a small bob, *Journal of Engineering Mathematics*, **9**, 207–218, (1975).

6. Schafer, B. Free vibrations of a gravity-loaded clamped-free beam, *Ingenieur Archiv*, **55**, 66–80, (1985).

7. Denoel, V. and Canor, T. Patching asymptotics solution of a cable with a small bending stiffness, *Journal of Structural Engineering*, **139**, 180–187, (2013).

8. Alben, S. and Shelley, M. J. Flapping states of a flag in an inviscid fluid: bistability and the transition to chaos, *Physical Review Letters*, **100**, 074301, (2008).

9. Shelley, M. J. and Zhang, J. Flapping and bending bodies interacting with fluid flows, *Annual Review of Fluid Mechanics*, **43**, 449–465, (2011).

10. Allen, J. J. and Smits, A. J. Energy harvesting eel, *Journal of Fluids and Structures*, **15**, 629–640, (2001).

11. Liao, J. C., Beal, D. N., Lauder, G. V. and Triantafyllou, M. S. Fish exploiting vortices decrease muscle activity, *Science*, **302**, 1566–1569, (2003).

12. Michelin, S. and Llewellyn Smith, S. G. Resonance and propulsion performance of a heaving flexible wing, *Physics of Fluids*, **21**, 071902, (2009).

13. Huang, L. Mechanical modeling of palatal snoring, *Journal of the Acoustical Society of America*, **97**, 3642–3648, (1995).

14. Sarradj, E., Fritzsche, C. and Geyer, T. Silent owl flight: bird flyover noise measurements, *AIAA Journal*, **49**, 769–779, (2011).

15. Manela, A. Vibration and sound of an elastic wing actuated at its leading edge, *Journal of Sound and Vibration*, **331**, 638–650, (2012).

16. Huang, W.-X. and Sung, H. J. Three-dimensional simulation of a flapping flag in a uniform flow, *Journal of Fluid Mechanics*, **653**, 301–336, (2010).

17. Alben, S. Optimal flexibility of a flapping appendage in an inviscid fluid, *Journal of Fluid Mechanics*, **614**, 355–380, (2008).

18. Manela, A. and Howe, M. S. The forced motion of a flag, *Journal of Fluid Mechanics*, **635**, 439–454, (2009).

19. Datta, S. K. and Gottenberg, W. G. Instability of an elastic strip hanging in an airstream, *Journal of Applied Mechanics*, **42**, 195–198, (1975).

20. Lemaitre, C., Hemon, P. and de Langre, E. Instability of a long ribbon hanging in axial air flow, *Journal of Fluids and Structures*, **20**, 913–925, (2005).

21. Saffman, P. and Baker, G. Vortex interactions, *Annual Review in Fluid Mechanics*, **11**, 95–122, (1979).

22. Sarpkaya, T. Computational methods with vortices – the 1988 freeman scholar lecure, *Journal of Fluids engineering*, **11**, 5–52, (1989).

23. Manela, A. and Huang, L. Point vortex model for prediction of sound generated by a wing with flap interacting with a passing vortex, *Journal of the Acoustical Society of America*, **133**, 1934–1944, (2013).